Morphological, electronic, and magnetic properties of multicomponent cobalt oxide nanoparticles synthesized by high temperature arc plasma

Morphological, electronic, and magnetic properties of multicomponent cobalt oxide nanoparticles synthesized by high temperature arc plasma

Arkaprava Das[1], C. Balasubramanian[1,2*], Prachi Orpe[1,3], G. M. Pugliese[4], Alessandro Puri[5], Augusto Marcelli[6,7,8], Naurang Saini[4]

[1]*Atmospheric Plasma Div., FCIPT campus, Institute for Plasma Research, Gandhinagar-382016, India*
[2]*Homi Bhabha National Institute, Mumbai, Maharashtra-400 094, India*
[3]*Department of Physical Science, Institute of Science, Nirma University, Ahmedabad 382 481, India*
[4]*Sapienza Università di Roma, P.le Aldo Moro 2, I-00185, Rome, Italy*
[5]*CNR-IOM-OGG c/o ESRF – The European Synchrotron, 71 Avenue des Martyrs, 38000 Grenoble, France*
[6]*INFN - Laboratori Nazionali di Frascati, Via E. Fermi 54, 00044 Frascati (RM), Italy*
[7]*CNR - Istituto Struttura della Materia and Elettra-Sincrotrone Trieste Basovizza Area Science Park 34149, Trieste, Italy*
[8]*RICMASS, Rome International Center for Materials Science Superstripes, Via dei Sabelli 119A, 00185 Rome, Italy*

Abstract

Many technological applications demand for large amount of nanoparticles with well-defined magnetic properties, which target is feasible only by using large-scale production methods. In this framework, we have performed structural and local geometric investigations of cobalt oxide nanoparticles synthesized by high temperature arc plasma route in helium and in air atmosphere with different arc currents, a competitive and low cost technological approach to synthesize large quantity of different types of nanoparticles. The complex scenario of phase fraction, shape, size distribution and hysteresis loop features of high temperature arc plasma synthesis of nanoparticles can be determined by the arc current and the selected gas. The X-ray diffraction (XRD) patterns describe a multicomponent phase formation containing cubic cobaltous oxide (CoO), cobaltic oxide (Co_3O_4) and metallic cobalt phases. The synthesis of different phases is confirmed by X-ray absorption spectroscopy (XAS) measurements at the Co *K* edge. Actually, both Extended X-ray absorption fine structure (EXAFS) and X-ray absorption near edge structure (XANES) analyses show the presence of metallic nanoparticles in He ambience at high arc current. Moreover, high-resolution transmission electron microscopy (HRTEM) images and magnetic hysteresis loop measurements show that the mean particle size increases and the coercivity reduces with increasing arc current in air ambient due to the intense particle-particle interaction. At variance, in helium atmosphere synthesized samples due to the high quenching rate and the high thermal conductivity, a multi-domain formation in which the nanoparticles crystalline fraction decreases and a fluctuating coercivity due to core-shell structure is observed.

Key words: Arc Plasma; Cobalt oxide nanoparticles**;** X-ray diffraction pattern (XRD); Extended X-ray absoprtion fine strcuture (EXAFS); X-ray Absorption Near Edge Structure (XANES)

**Author for correspondence:* balac@ipr.res.in

1. Introduction:

Nanometer-sized semiconductors, metallic and dielectric materials attract a large interest due to their advantages in the fabrication of magnetic, electronic and optical devices. However, when any material is reduced to nanometer dimensions, an interplay among different physical and chemical interactions occur, and new properties may emerge [1]. As an example, compared to their bulk counter-parts, magnetic cobalt and iron oxides nanoparticles exhibit a higher coercivity and squareness because of their high surface to volume ratio [2].

Magnetic nanoparticles have attracted significant attention in last few decades for their unique mesoscopic properties and applications [3–5], e.g., in opto-electronics where in comparison to two-dimensional (2D) arrays, small magnetic domains may gain advantages from the collective behavior of a dense nanostructure. Moreover, other nanostructured systems like nanorods, nanoribbons, nanowires, etc., can be used to fabricate devices [6–8]. Nanostructures, are typically characterized by their interaction processes, long-range periodicity and homogeneity. Moreover, the number of atoms of a cluster mainly drives overall collective behavior. For instance, the ionization potential of an atom and the work function of a solid composed of the same atom are different [1]. Starting from these considerations, many applications need large-scale synthesis methods of nanoparticles and, in particular, of magnetic nanoparticles [9].

Growth of Co nanoparticles is interesting due to their potential applications in various fields, e.g., rechargeable batteries, [10,11] Co based sensors, [12] materials for abatement catalyst of Co [13], etc. Another relevant application of Co nanoparticles is in turbine engine magnetic bearing due to their high saturation magnetization, low coercivity, high Curie temperature and high permeability [14]. However, Co nanoparticles easily oxidize in the presence of oxygen, and the amount of oxide affects their magnetic properties. Two main phases of CoO exists: the face centered cubic (fcc) rocksalt phase with the space group $Fm\bar{3}m$, the more stable, in which Co^{2+} is octahedrally coordinated and the hexagonal closed packed (hcp) wurtzite phase, $P6_3mc$, in which Co^{2+} is tetrahedrally coordinated [15]. The production of pure CoO nanoparticles is a complex procedure because of the concurrent synthesis of Co_3O_4 and other metallic phases [16]. Metal nanoparticles always exhibit a higher saturation magnetization compared to oxide nanoparticles [17]. This property represents a great advantage for biomedical applications like hyperthermia [18]. However, in some synthesis procedures, a few nm thick oxide layer, which behaves as a

passivation layer preventing further oxidation, has been observed at the surface of metallic nanoparticles [19].

At present, synthesis of large amounts of metal oxide and nitride nanoparticles is possible using the high temperature thermal arc plasma process. In the thermal plasma, the available high enthalpy accelerates the reaction kinetics and a subsequent rapid quenching occurs due to the sharp temperature gradient. This mechanism can be tuned to synthesize the desired nanoparticle phases. Several reports are available in literature for the synthesis of aluminum oxide, titanium oxide, iron oxide, aluminum nitride and other nano-materials [20–25]. The main advantage of this method is that it doesn't require a post synthesis process to control and improve the crystalline phase of nanoparticles. We have used in the past the thermal plasma method to synthesize Co nanoparticles and discussed the formation of CoO with formation enthalpy of ~ -237.9 kJ/mol and of Co_3O_4 with formation enthalpy of ~ -891.0 kJ/mol, [14] controlling the heat generated by the plasma inside the synthesis chamber.

In this manuscript we report the synthesis of cobalt oxide nanoparticles in air and in helium atmosphere. In particular, we present the synthesis of mixed phases of CoO (cobaltous oxide), metallic Co and Co_3O_4 (cobaltic oxide) and discuss the impact of the different atmospheres on the reaction kinetics. The synthesis process starts from the vaporization of the target material and the subsequent condensation, which leads to highly ordered nanoparticles phases, induced by the sharp temperature gradient. We have in particular investigated the role of the arc current and of the different gas (air and He) to shape, size, local structure and stoichiometry of the synthesized nanoparticles with the aim to optimize the synthesis parameters for a large-scale production. Results have been obtained combining Transmission Electron Microscopy (TEM) for the morphological study, X-ray diffraction (XRD) for the structural study and X-ray absorption spectroscopy (XAS) for the local structure investigation while vibrating sample magnetometry (VSM) has been used for the characterization of the magnetic properties. Finally, XAS spectroscopy and simulations at the Co *K* edge has been performed to demonstrate that at higher arc current and in helium environment, the synthesis of the metallic Co nanophase is particularly effective.

2. Experimental:

Cobalt oxide (CoO) nano-powder has been synthesized using the direct current (DC) thermal arc plasma method where graphite was used as cathode and commercial micron size cobalt powders (Sigma Aldrich product no 266647) as anode. An IGBT based 300 V - 15 A DC power supply was used for plasma generation. During arcing the electrodes were separated by a distance of 5 to 10 mm in a vacuum chamber which was evacuated to ~10^{-2} mbar and then filled with different ambient gas. The nanoparticles were synthesized at three different arc currents: 50 A, 100 A and 150 A both in air (samples named as Air50, Air100 and Air150) and in He (samples named as He50, He100 and He150) atmosphere. Therefore, six different nano-powder samples synthesized under the same operating conditions have been investigated. DC voltage, applied between the electrodes, was varied from 25 V to 50 V by adjusting the distance between electrodes. The high temperature of the arc plasma led to melting of the anode material (cobalt). As the ionized Co plasma radially moves away from the plasma column, the temperature falls sharply due to a high cooling rate of ~10^6 K/s near the anode surface. This allows also the formation of neutral Co atom clusters. Inside the chamber, the process lasts until thermal non-equilibrium conditions remain, and the nanoparticles generated from the process move towards the chamber walls and get settled there. After cooling, powders are removed from the walls of the chamber for the experimental characterizations [14].

Powder X-ray diffraction for the phase identification of ordered phases had been performed with the X-ray diffractometer Bruker AXS D8 using Cu-K_α radiation and a Ni filter. 2θ patterns were recorded in the range 10° to 90° with step size of 0.05°. XAS experiments for the local structure analysis such as X-Ray Absorption Near Edge Structures (XANES) and Extended X-ray absorption fine structure (EXAFS) were carried out in transmission mode at the LISA beamline of the European Synchrotron Radiation Facility (ESRF) in Grenoble (France). At LISA the Si(311) monochromator was used with the higher order harmonics filtered out by both a crystal detuning and using Si mirrors [26] . A standard transmission x-ray absorption setup was used to record spectra on the samples and references. For the measurements of the powder samples a suspended solution was prepared. Ultra-sonicated powders were subsequently deposited on a cellulose membrane [27]. All spectra were collected at room temperature and repeated three to four times with a Co metal reference foil acquired simultaneously to cross check the reproducibility of the

spectra and to calibrate the energy. Transmission Electron Microscopy (TEM) measurements were performed using FEI Tecnai G2 300 kV for morphological studies. For these experiments, nanoparticles were dispersed onto a 400 mesh carbon film coated Cu grid. For magnetic measurements the Lakeshore 7404 vibrating sample magnetometer (VSM) was utilized to collect the magnetization hysteresis loops of all powder samples.

3. Results and discussions:

3.1 Crystal structure studies:

Figure 1 (a) and 2 (a) compare XRD powder diffractograms of three samples synthesized in air: Air50, Air100, Air150 and of the other three synthesized in He atmosphere: He50, He100, He150. For those synthesized in air, diffraction peaks mainly correspond to the cubic CoO (cobaltous oxide) phase (JCPDS PDF-71-1178). However, a weak peak at 44.7° points to a contribution of cubic metallic Co (111) (JCPDS PDF-15-0806). For sake of clarity, we have stack-plotted the XRD patterns in Figure SF-1 (Electronic Supplementary Information) file for all Co species formed in our synthesis process. The most intense peak in the XRD pattern for the cubic Co phase appears at 44.3°. So, the presence of this weak feature at 44.7° is consistent with a small amount of the metallic Co phase. Looking at the reference XRD patterns, the most intense (311) peak of the Co_3O_4 (cobaltic oxide) (JCPDS PDF-76-1802) and the (111) of the CoO have 2θ positions very close to each other, *i.e.,* at 36.5° and 36.6°, respectively. These contributions cannot be resolved and we observe only one intense and broad peak at ~36.5° in all XRD patterns of these samples. However, other reflections, i.e., (200), (220), (311), (222) are detectable at 42.5°, 61.7°, 73.8°, 77.7°, pointing to the formation of the cubic CoO phase while the (220), (511), (440) peaks at 31.4°, 59.4°, 65.4° belong to the Co_3O_4 phase. Moreover, in the magnified panel in Figure 1(b), another peak appears in the pattern collected under air atmosphere. The feature at 36.9° is lacking or too weak to be detectable in the XRD patterns (Figure 2(b)) of samples synthesized in He ambient and is assigned to the cobalt nitride phase [28]. Indeed, the amount of nitrogen present at the base vacuum of 10^{-2} mbar is sufficient to form cobalt nitride.

For samples synthesized in helium, XRD patterns (Fig. 2) show the presence of CoO and of a strong cubic metallic Co phase, which increases concurrently with arc current value. At 150 A the most intense Co peak (111) is detected at 44.2° while two other peaks: (200) and (220) at 51.5° and 76°, also appear. The presence of Co_3O_4 is negligible in XRD patterns collected in helium.

Since the incident flux at the Cu K_α of the laboratory source is limited, it is probably not sufficient to resolve any weak phase. However, the magnified pattern in the 2θ range 34.8°-38.4° in Figure 2(b) does not show additional features ruling out the formation of the cobalt nitride phase. On the contrary, as discussed later, X-ray absorption spectroscopy, probing the local structure of ordered and not ordered phases, is able to detect signatures of many weak phases.

The average crystallite size for all XRD patterns has been calculated using the (200) reflection of the CoO phase. It increases with the arc current for both air and He ambient. However, the increase is more pronounced in air (from ∼35 nm to ∼40 nm) than in helium. The values of the crystallite size are listed in Table ST-1 (Electronic Supplementary Information).

We also observed a peak shift towards higher 2θ value i.e., ~0.1° for Air150 sample as compared to Air50 sample. Although small, the shift provides a direct evidence of a compressive strain generated by the thermal stress associated to the sharp temperature gradient in the samples [29]. The shift is not observed in the samples synthesized in He atmosphere. Indeed, at a given pressure, the mean free path is higher in the He atmosphere compared to air and, as a consequence, the collision cross section for producing the avalanche breakdown is lower. This mechanism leads to a reduced thermal stress in the He atmosphere. A higher quenching rate in He might lead also to the reduced evaporation rate from the plasma plume [30]. Consequently, because the particle-particle interaction is higher in air, evaporation rate and stress are both higher [31].

During the synthesis, a large number of Co atoms leave the molten plasma zone, further nucleate forming Co clusters with other oxides. Compared to air, the partial pressure and the availability of oxygen atoms are lower in the He atmosphere. At higher arc currents, this results in the formation of metallic Co species. Since the formation enthalpy of solid metallic Co is higher than CoO (-7.04 kJ/g) and Co_3O_4 (-26.84 kJ/g), its formation occurs with the highest probability at high values of the arc current (calculations for the reaction enthalpy of CoO and Co_3O_4 are given in Electronic Supplementary Information). The highest amount of the Co_3O_4 phase is expected at 150 A for both He and air ambience due to the higher plasma enthalpy. However, as the temperature increases, it affects significantly the morphology, the local order and the stoichiometry of the synthesized products.

3.2 The local structure studies:

The Co K-edge x-ray absorption near edge structure (XANES) for Air and He series samples for different arc currents (50, 100, 150 A) are compared in Figure 3(a) and 3(b) respectively. The inset in Figure 3(a) shows a magnified view of the pre-edge features of the Air series. Likewise, the inset in Figure 3(b) shows the comparison of the pre- edge features of the He series. The Co *K* edge spectrum can be described by a transition from the 1*s* to empty states to dipole allowed local partial empty density of states of *p* symmetry over the Fermi energy [32]. Differences in the spectra can be associated to changes in the empty local density of states in the continuum, i.e., triggered by differences in the local geometrical structures. In the XANES spectra of Co powders we mainly recognize three features: A, B and C for the Air series samples, and increasing the arc current we do not observe any significant change nor shifts of pre and post edge features. In the lower panel of Figure 3(a) the differences among spectra are plotted for Air100 and Air150 with respect to Air50. The difference spectra point out a small intensity enhancement of the B feature for both Air100 and Air150 samples. The results indicate that the Co phases are hardly affected by the non-equilibrium thermal synthesis process. On the other hand, XANES spectra collected in the He atmosphere show significant changes in the B feature as well as in its position. The change in the intensity is outlined in the difference spectra in the lower panel and regards both B and C features and the absorption edge. The shift of the spectral weight towards higher energy can be associated to the presence of different Co species whose relative amounts changes with the arc current [14].

Apart from the features B and C, the pre-edge described by $1s \rightarrow 3d$ quadrupole and $1s \rightarrow 4p$ dipole transitions [14] occurs at 7710.5 eV. The latter being due to structural distortions around the metal in the octahedral site [33]. We will come back to discuss this in the next section. The pre-edge feature in the XANES of the Air series does not show any change with the arc current, neither in position nor in intensity (Fig. 3a). At variance, a significant change with the arc current occurs in the samples of the He series (Fig. 3b).

Figure 4 (a) and 4(b) show the k^3 - weighted EXAFS oscillations extracted from the absorption spectra measured on the samples of the Air and He series. Differences in the EXAFS oscillations of Air and He series can be recognized. While minor changes are observed on the EXAFS oscillations of the Air series with the arc current, spectra of the He series show a large effect. This is consistent with XANES spectra pointing out large variations in the local geometry including

Co-O and Co-Co bond lengths for the He series. Likewise, there is no significant difference in the Fourier Transform (FT) of the corresponding EXAFS signals of the Air series samples, while for the He series a large variation with the arc current is evident, as shown in Fig. 5(a) and 5(b), respectively. The FT performed in the *k* range 3.4-14 $Å^{-1}$ using a Gaussian window provides real space information describing the atomic distribution around the Co atoms. The peak observed between 1-2 Å reflects the Co coordination with the nearest O atoms of the first shell (Co-O), whereas several shells are resolved above 2 Å, associated to the Co-Co and Co-O scattering processes [14]. A significant evolution in the FTs for the He series and a splitting of the second coordination shell can be recognized Fig. 5(b).

The EXAFS oscillations were modeled using the EXCURVE 9.275 code with calculated backscattering amplitude and phase shifts [34]. A six shells model was used where the near-neighbor distances (R_i) and the related Debye-Waller factors were the fit parameters. For each DC current the coordination numbers (N_i) were kept fixed after fit trials in order to obtain the percentages of the different cobalt phases. The amplitude reduction factor (S_0^2 = 0.8 and 0.9 for oxygen and cobalt atoms, respectively) and the photoelectron energy zero (E_0 = -3.839 eV in air, E_0 = -3.278 eV in He) were kept fixed for the refinements. The starting parameters obtained from the XRD analysis were the input parameters for the six shells model. We considered the Co-O ($R_{Co\text{-}O}$ = 1.93 Å) and the Co-Co contributions ($R_{Co\text{-}Co}$ = 3.01 Å) for the CoO phase, the Co-Co contribution ($R_{Co\text{-}Co}$= 2.49 Å) for the metallic Co phase, the Co-O bond distance $R_{Co\text{-}O}$=2.14 Å) and two Co-Co contributions $R_{Co\text{-}Co}$ = 2.87 Å, $R_{Co\text{-}Co}$= 3.37 Å) for the Co_3O_4 phase. The number of independent data points for the least square fit was $2\Delta k\Delta R/\pi \sim 20$ for Δk-range and ΔR-range being 10.6 $Å^{-1}$ and 3 Å, respectively. Figures 5(a) and 5(b) display the best fit for the amplitude of $\chi(R)$, *i.e.*, the FT of the k^3 - weighted $\chi(k)$ spectra of the Air and He series.

The EXAFS fit of the Air50 returns a mixture containing CoO (~61.3%), Co_3O_4 (~35%) and a small amount of metallic Co (~3.7%). Considering the XRD patterns, we have performed this fit only considering the cubic phases of all aforementioned Co species. The XRD pattern of the Air50 shows a small Co_3O_4 phase that increases with the arc current reaching a maximum ~50%, whereas the metallic Co phase fraction increases to ~7% for the Air150 sample. Actually, from the FT in Figure 5(a), the change in the atomic distribution around the Co atom as a function of DC current is negligible. Unlike the Air series, as shown in Fig. 5(b) the FT of He series shows a substantial

change with the arc current. The evolution can be attributed to the different phases present in these samples. For the He50 sample, looking at the sharp peak at ~36.5° in the XRD pattern, we can identify a single phase (CoO). At higher currents the intensity of the peak at ~36.5° containing both the contributions of the (311) peak of the Co_3O_4 phase and the (111) peak of the CoO phase decreases. Indeed, from the fits shown in Figure 5 (a,b) the best fit is obtained when the partial phase fraction of the Co_3O_4 remains more or less constant, whereas the percentages of the CoO phase decreases at the cost of metallic Co phase. The best quality of the fit for this batch of nanoparticles is obtained including also the Co-Co shell contribution at $R_{Co\text{-}Co}$= 3.52 Å for the Co_3O_4 phase. The highest metallic Co phase fraction obtained by the EXAFS analysis is 30% for the He150 sample, in qualitative agreement with XRD results. In Table ST2 the simulated local structure parameters are summarized for Air and He series samples.

Actually, at higher arc currents, as one moves away from the plasma plume towards the walls of the chamber, the temperature gradient is steeper. As a consequence, a substantial amount of metal vapor is produced at a faster rate near the molten metal mixture (the anode) and, in the He environment it does not encounter sufficient oxygen atoms to oxidize. Accordingly, a further nucleation takes place due to the high initial speed of the evaporation process. This might be the reason of the enhancement of the metallic Co phase while increasing the arc current in He. Incidentally, the XRD pattern for the He100 sample reveals a small presence of the metal Co phase. We can explain this behavior as due to the presence of oxygen vacancies at this arc current value, as already confirmed from the EDAX analysis [35]. At 50 A arc current, the flux density of the outgoing atoms is lower compared to the 100 A arc current with the oxidation of all metallic Co atoms in the 50 A sample. However, for larger atomic fluxes, e.g., for 100 A, all Co atoms are not oxidized with the proper stoichiometric ratio for monoxide and trioxide phase. This explains the presence of oxygen vacancies in the He100 sample. However, at 150 A, due to increased plasma enthalpy the area for the homogenous nucleation surrounding the plume zone increases and monoxide and trioxide phases are formed without oxygen vacancies. This result will be discussed later in the context of the anomalous magnetic behavior of the coercivity values of these samples.

3.3 Morphological analysis:

Figure 6(a-c) and 10(a-c) show TEM micrographs of all samples studied in this work. Magnified images of the samples synthesized in air and He atmosphere are shown in Figure 7(a-c) and 11(a-

c), respectively. In a previous investigation we have used HRTEM images of the same series [14] to calculate the particle size distributions. Actually, due to the availability of a higher formation enthalpy, increasing the arc current also increases the mean particle size as growth of the particles continues after nucleation. However, since the ambient temperature is much lower than the temperature of the plasma plume, diffusion reaction cannot take place [36,37].

The mean particle dimensions were calculated from the histogram after a Gaussian distribution fit. Figure 8(a-c) and 12(a-c) shows the particle size distributions for Air50, Air100, Air150 and He50, He100, He150 samples, respectively. When compared to air, due to the higher quenching rate, the increase in the mean particle size is lower in the He atmosphere [30,38]. The size distribution and the mean size of particles were calculated using the ImageJ software considering ~300 particles. Data are presented in Table ST3 with the corresponding standard deviation values. The particle size of spherical and polygonal objects varies from ∼10 nm to ∼130 nm for all distributions.

The unit cell volume of the cubic CoO, Co_3O_4 and metallic Co are 76.22 $Å^3$, 541.44 $Å^3$ and 44.52 $Å^3$, respectively. From the EXAFS analysis, we point out the increase of the Co_3O_4 vs. the arc current. In air, the enhancement of the Co_3O_4 phase fraction takes place at the cost of the CoO phase with an increase in the mean particle diameter and with a broader size distribution. However, the particle size increase is lower in the helium atmosphere since a significant amount of the metallic Co phase, characterized by a smaller unit cell volume, is present.

The enhanced contribution of the metallic Co phase at higher arc currents, with a more ordered structure respect to the CoO and Co_3O_4 phases seems to reduce the structural disorder. Increasing the arc current in He atmosphere may reduce the asymmetry of the nanoparticle shape. In fact, a large number of symmetric nanoparticles is present in the images of the samples synthesized in He. Another important parameter which influences the nanoparticles morphology is the thermal conductivity of the ambient. At room temperature, thermal conductivity is 0.026 Watt/m-K and 0.15 Watt/m-K in air and He, respectively and both increase with temperature. Therefore, while in air the sharp temperature gradient does not give time for the symmetric growth of nanoparticles; however, in He atmosphere, due to the higher thermal conductivity of He, nanoparticles grow more symmetrically. This behavior is confirmed from the magnified TEM micrographs in Figure 7 showing that nanoparticles synthesized in air have mainly square or rectangular shapes and few

spherical particles, while nanoparticles synthesized in helium (Figure 11) are mostly spherical with few distorted hexagonal contributions.

The presence of both XRD patterns and atomic planes in TEM images confirm the crystalline nature of these nanoparticles. The atomic planes observed in Figure 9(a-c) for the Air series samples and the corresponding inter-planar spacing have been calculated using the Gatan Digital Micrograph software from the inverse Fast Fourier transformation (FFT) of the intensity line profile (not shown in the manuscript). The same lattice fringes are shown for the He series in Figure 13(a-c). All values given in the figures are consistent with the reflections of the XRD patterns. For example, for Air150 and He100 sample, the *d* spacings are 0.24 nm and 0.20 nm, respectively, which are the *d* spacing values of the (111) reflection of the CoO and the (111) reflection of the metallic Co, respectively. This correlation directly confirms the presence of both CoO and metallic Co phases. The values of the *d* spacing calculated from the reference XRD patterns are listed in Table ST4 (Electronic Supplementary Information), where the corresponding planes are also highlighted. For the He150 sample, the calculated *d* spacing is 0.19 nm, which corresponds to the (331) reflection of the Co_3O_4 phase. However, this reflection is masked in the XRD pattern by the intense metallic Co (111) contribution. Due to closer inter-planar spacing, sometime it is indeed difficult to recognize the occurrence of different phases.

In Figure 11(c) the TEM image of the He150 sample shows an oxide layer around the spherical nanoparticles, not present in other samples. As the amount of the metallic Co is the highest in this sample, we hypothesize that this oxide layer of ~2 nm thick is mainly due to cobalt oxide. In a base vacuum of 10^{-2} mbar pressure, the dissociative oxygen absorption starts to take place with an electronic exchange among Co^{2+} and oxygen atoms. As a consequence, due to the electronic exchange a Co^{2+} cation vacancy generation takes place simultaneously with the availability of Co^{3+} cations.

3.4 Magnetic properties study:

Figure 14(a) and 14(b) show the magnetization curves for the samples synthesized in Air and He atmosphere for all arc currents. The values in Table 1 for the saturation magnetization (M_s) and the magnetic coercivity (H_c) were calculated from *M vs. H* loops for all samples. In the insets, are shown the magnified views of the magnetic coercivity. From experimental values it can be observed that nanoparticles synthesized in helium exhibit better magnetic properties. In both gases

M_s (emu/g) increases with the arc current and H_c (Oe) reduces, except for the case of the He100 sample. Indeed all samples but He100 show an increment of the saturation magnetization in both atmospheres. This might be explained and correlated with the cationic distribution, the presence of dead layer or non-magnetic surface layers [39]. In addition to the ambient gas, magnetic properties are affected by particle dimensions [40]. Usually, larger and coarser nanoparticles exhibit a higher M_s compared to finer ones, a result valid in the present scenario [39]. The reduced value of M_s for smaller nanoparticles is due to the large surface area (for a given volume) and to surface molecules contributing to the magnetization. Indeed, both the presence of a non-magnetic surface layer or spin canting effects within the outer layer [34] may reduce M_s. Neglecting the presence of non-magnetic surface layers because they are not observed in our samples except in the He150 sample, the spin canting effect might be the source of the small M_s value associated with the smallest particles [41]. However, this effect is mainly a low temperature phenomenon and cannot explain the reduced M_s value at lower arc current as pointed by Nawale *et al*., while a high crystallinity is consistent with a high M_s [9]. At low arc current, due to reduced number of magnetic domains present in the smallest particles, a smaller magnetic field is required to align all existing domains while for large particles, the presence of a multi-domain structure requires a much higher magnetic field to reach the saturation level. This mechanism may lead to an increased M_s value vs. the arc current and to a high crystallinity.

Magnetic properties also depend on stresses in the system. Due to the thermal stress inside the lattice, the particle-particle interaction reduces H_c [42]. XRD patterns of the Air series samples points out the presence of strains, which from the hysteresis curves are compatible with a reduced H_c value. Indeed, Koushika *et al*. showed that particle distribution following a particular trend or aligned in a particular direction results in a lower H_c [42]. Our HRTEM images don't show any particular alignment of nanoparticles. However, increasing the arc current, the average particle size increases and H_c reduces. As a consequence, we hypothesize the existence of multi-domains as the result of a dipole-dipole interaction [43].

The multi-domains formation not only reduces the coercive force, but also decreases the magnetic energy [44]. From XRD patterns, we observe that the He100_sample contains a small amount of metallic Co species and probably a high number of oxygen vacancies. The presence of the latter would relatively increase the stoichiometric proportion of Co, which also supports the increased

H_c value [35]. The increment in the coercive value can be justified by the presence of this metallic Co phase. A reduction in H_c is observed for the He150 sample, but its metallic Co phase fraction increases to 21.4%. Such kind of shell structure always affects the magnetic properties. In this case, the presence of a thick CoO surface layer around the nanoparticle showed in the HRTEM image of this sample in Figure 11(c) is probably at the origin of the reduction of the coercive field. In air, H_c decreases consistently while increasing the arc current and no core shell type structure is detected as demonstrated by the HRTEM images of these samples [45].

During the synthesis process, when metal atoms come closer and starts to form clusters, the discrete atomic localized orbitals of any individual atom starts to delocalize and changes in the energy band structure may occur [46]. Therefore, increasing the arc current, the interplay between emerging higher ordering and delocalization of Co 3*d* orbitals will affect the magnetic properties of the nanoparticles. It is reported that for Co_3O_4 spinel structure, any distortion in the Co environment might change charge and spin state of the Co^{3+}, a mechanism which subsequently affects the overlap between O^{2-} and Co^{3+} orbitals [47]. Finally, the changes in the orbital hybridization actually modulate the internal local magnetic fields of the Co_3O_4. Since this phase is present in all samples, both H_c and M_s would be affected. We have also to consider the presence of the antiferromagnetic exchange interaction in the Co_3O_4 structure among Co^{3+} and Co^{2+} ions located at octahedral and tetrahedral sites, respectively, which is also tuned by the synthesis conditions [4]. Summarizing, the amount of the Co_3O_4 phase will certainly tune the magnetic properties of these nanoparticles, but an exhaustive quantitative discussion is beyond the scope of this contribution and requires further experimental synthesis and analysis.

Conclusion:

The thermal DC arc plasma has been used to synthesize cobalt oxide nanoparticles. This research shows that the gas used for the synthesis has a great impact on the formation of nanoparticle species, in particular to control the formation of multicomponent species. In particular, nanoparticles synthesized under a He ambient are less ordered and crystalline, but exhibit well defined magnetic properties. The presence of a higher amount of metallic cobalt together with other cobalt (II,III) oxide species is typical of the synthesis in helium. The presence of metallic Co is evident by the XRD patterns and is confirmed by the EXAFS analysis. However, it is not straightforward to quantify the phase fraction of any individual Co species and their actual particle

size distribution. For both He and air environments, ordered and crystalline fractions increase with the arc current because the higher enthalpy induces both a multiple nucleation and growth processes. However, compared to air, the growth is lower in He due to its higher quenching rate. Increasing the arc current, due to the high atomic flux, the particle-particle interaction and the growth of non-magnetic surface oxide layers, the hysteresis loop appears not correlated in helium, in particular at the higher value of the arc current. Moreover, the magnetic coercivity of the NPs is lower in air.

All results are consistent and in good agreement with the available researches published on cobalt nanoparticles. The experimental synthesis scenario described in this manuscript represents an advanced starting point to identify and select the parameters required for large-scale production of nanoparticles with well-defined magnetic properties as required by particular technological applications. [11]

Acknowledgements:

The authors acknowledge the financial support of the Bilateral Cooperation Agreement between Italy and India of the Italian Ministry of Foreign Affairs and International Cooperation (MAECI) and the Department of Science and Technology (DST), India, in the framework of the project of major relevance '*Investigating local structure and magnetism of Co nanostructures*'. CB also acknowledges DST and JNCASR, India for providing travel support through DST-Synchrotron-Neutron Project to perform the experiments at ESRF. AD acknowledges the Institute for Plasma Research for the post-doctoral fellowship. Authors also acknowledge the experimental help extended by E. Paris during the first phase of this activity.

References:

[1] F.S. Denes, S. Manolache, Y.C. Ma, V. Shamamian, B. Ravel, S. Prokes, Dense medium plasma synthesis of carbon/iron-based magnetic nanoparticle system, J. Appl. Phys. 94 (2003) 3498–3508.

[2] J.H. Fendler, Nanoparticles and nanostructured films: preparation, characterization, and applications, John Wiley & Sons, 2008.

[3] S.A. Makhlouf, Magnetic properties of Co3O4 nanoparticles, J. Magn. Magn. Mater. 246 (2002) 184–190.

[4] Y. Koseoglu, F. Kurtulus, H. Kockar, H. Guler, O. Karaagac, S. Kazan, B. Aktas, Magnetic characterizations of cobalt oxide nanoparticles, J. Supercond. Nov. Magn. 25 (2012) 2783–2787.

[5] F. Taghizadeh, Fabrication and investigation of the magnetic properties of Co and Co3O4

nanoparticles, Opt. Photonics J. 6 (2016) 62.

[6] L.D. Burke, M.E. Lyons, O.J. Murphy, Formation of hydrous oxide films on cobalt under potential cycling conditions, J. Electroanal. Chem. Interfacial Electrochem. 132 (1982) 247–261.

[7] L.N. Lewis, Chemical catalysis by colloids and clusters, Chem. Rev. 93 (1993) 2693–2730.

[8] A.K. Singh, Q. Xu, Synergistic catalysis over bimetallic alloy nanoparticles. ChemCatChem 5: 652–676, (2013).

[9] A.B. Nawale, N.S. Kanhe, K.R. Patil, S. V Bhoraskar, V.L. Mathe, A.K. Das, Magnetic properties of thermal plasma synthesized nanocrystalline nickel ferrite (NiFe2O4), J. Alloys Compd. 509 (2011) 4404–4413.

[10] F. Lichtenberg, K. Kleinsorgen, Stability enhancement of the CoOOH conductive network of nickel hydroxide electrodes, J. Power Sources. 62 (1996) 207–212.

[11] Z. Wang, L. Wang, S. Liu, G. Li, X. Gao, Conductive CoOOH as Carbon-Free Sulfur Immobilizer to Fabricate Sulfur-Based Composite for Lithium–Sulfur Battery, Adv. Funct. Mater. 29 (2019) 1901051.

[12] H. Yamaura, K. Moriya, N. Miura, N. Yamazoe, Mechanism of sensitivity promotion in CO sensor using indium oxide and cobalt oxide, Sensors Actuators B Chem. 65 (2000) 39–41.

[13] H.-K. Lin, H.-C. Chiu, H.-C. Tsai, S.-H. Chien, C.-B. Wang, Synthesis, characterization and catalytic oxidation of carbon monoxide over cobalt oxide, Catal. Letters. 88 (2003) 169–174.

[14] P.B. Orpe, E. Paris, C. Balasubramanian, B. Joseph, S. Mukherjee, D. Di Gioacchino, A. Marcelli, N.L. Saini, Local structure of cobalt nanoparticles synthesized by high heat flux plasma process, Radiat. Phys. Chem. 137 (2017) 108–115.

[15] J.R. Singer, Magnetic susceptibility of NiO and CoO single crystals, Phys. Rev. 104 (1956) 929.

[16] A. V Ravindra, B.C. Behera, P. Padhan, O.I. Lebedev, W. Prellier, Tailoring of crystal phase and Néel temperature of cobalt monoxides nanocrystals with synthetic approach conditions, J. Appl. Phys. 116 (2014) 33912.

[17] N. Matoussevitch, A. Gorschinski, W. Habicht, J. Bolle, E. Dinjus, H. Bönnemann, S. Behrens, Surface modification of metallic Co nanoparticles, J. Magn. Magn. Mater. 311 (2007) 92–96.

[18] M. Zeisberger, S. Dutz, R. Müller, R. Hergt, N. Matoussevitch, H. Bönnemann, Metallic cobalt nanoparticles for heating applications, J. Magn. Magn. Mater. 311 (2007) 224–227.

[19] L. Smardz, U. Köbler, W. Zinn, Oxidation kinetics of thin and ultrathin cobalt films, J. Appl. Phys. 71 (1992) 5199–5204.

[20] C. Balasubramaniam, Y.B. Khollam, I. Banerjee, P.P. Bakare, S.K. Date, A.K. Das, S. V Bhoraskar, DC thermal arc-plasma preparation of nanometric and stoichiometric spherical magnetite (Fe3O4) powders, Mater. Lett. 58 (2004) 3958–3962.

[21] I. Banerjee, Y.B. Khollam, C. Balasubramanian, R. Pasricha, P.P. Bakare, K.R. Patil, A.K. Das, S. V Bhoraskar, Preparation of γ-Fe2O3 nanoparticles using DC thermal arc-plasma route, their characterization and magnetic properties, Scr. Mater. 54 (2006) 1235–1240.

[22] N. V Kulkarni, S. Karmakar, I. Banerjee, S.N. Sahasrabudhe, A.K. Das, S. V Bhoraskar, Growth of nano-particles of Al2O3, AlN and iron oxide with different crystalline phases in a thermal plasma reactor, Mater. Res. Bull. 44 (2009) 581–588.

[23] D. Zhang, G. Mylsamy, X. Yang, Z. Xie, X. Su, F. Liang, B. Yang, Y. Dai, High purity and good dispersity AlN nanoparticles synthesized by an arc discharge with assistance of direct nitridation, Ceram. Int. 47 (2021) 16972–16979.

[24] D. Zhang, Z. Xie, K. Zhang, H. Wang, T. Qu, W. Ma, B. Yang, Y. Dai, F. Liang, Y. Lei, Controlled regulation of the transformation of carbon nanomaterials under H2 mixture atmosphere by arc plasma, Chem. Eng. Sci. 241 (2021) 116695.

[25] Z. Tang, M. Hou, X. He, K. Ye, D. Zhang, Z. Xie, Y. Dai, F. Liang, Integrated purification of Gd and preparation of Gd2O3 nanoparticles by DC arc plasma, J. Rare Earths. (2021).

[26] S. Pascarelli, F. Boscherini, F. d'Acapito, J. Hrdy, C. Meneghini, S. Mobilio, X-ray optics of a dynamical sagittal-focusing monochromator on the GILDA beamline at the ESRF, J. Synchrotron Radiat. 3 (1996) 147–155.

[27] L. Signorini, L. Pasquini, L. Savini, R. Carboni, F. Boscherini, E. Bonetti, A. Giglia, M. Pedio, N. Mahne, S. Nannarone, Size-dependent oxidation in iron/iron oxide core-shell nanoparticles, Phys. Rev. B. 68 (2003) 195423.

[28] M.B. Lourenco, M.D. Carvalho, P. Fonseca, T. Gasche, G. Evans, M. Godinho, M.M. Cruz, Stability and magnetic properties of cobalt nitrides, J. Alloys Compd. 612 (2014) 176–182.

[29] G. Ouyang, W.G. Zhu, C.Q. Sun, Z.M. Zhu, S.Z. Liao, Atomistic origin of lattice strain on stiffness of nanoparticles, Phys. Chem. Chem. Phys. 12 (2010) 1543–1549.

[30] Z. Xue, C. Xinglei, C. Mo, Z. Guofu, Thermodynamic Properties and Transport Coefficients of Nitrogen, Hydrogen and Helium Plasma Mixed with Silver Vapor, Plasma Sci. Technol. 18 (2016) 560.

[31] N. Rahmani, R.S. Dariani, Strain-related phenomena in TiO2 nanostructures spin-coated on porous silicon substrate, Superlattices Microstruct. 85 (2015) 504–509.

[32] C. Gougoussis, M. Calandra, A. Seitsonen, C. Brouder, A. Shukla, F. Mauri, Intrinsic charge transfer gap in NiO from Ni K-edge x-ray absorption spectroscopy, Phys. Rev. B. 79 (2009) 45118.

[33] A. Juhin, F. De Groot, G. Vankó, M. Calandra, C. Brouder, Angular dependence of core hole screening in LiCoO 2: A DFT+ U calculation of the oxygen and cobalt K-edge x-ray absorption spectra, Phys. Rev. B. 81 (2010) 115115.

[34] J.J. Rehr, R.C. Albers, Theoretical approaches to x-ray absorption fine structure, Rev. Mod. Phys. 72 (2000) 621.

[35] P.B. Orpe, C. Balasubramanian, S. Mukherjee, Influence of DC arc current on the formation of cobalt-based nanostructures, Pramana. 89 (2017) 20.

[36] C. Balasubramanian, V.P. Godbole, V.K. Rohatgi, A.K. Das, S. V Bhoraskar, Synthesis of nanowires and nanoparticles of cubic aluminium nitride, Nanotechnology. 15 (2004) 370.

[37] C. Balasubramanian, B. Joseph, P.B. Orpe, N.L. Saini, S. Mukherjee, K. Dziedzic-Kocurek, J. Stanek, D. Di Gioacchino, A. Marcelli, Defective iron-oxide nanoparticles synthesised by high temperature plasma processing: a magnetic characterisation versus temperature, Nanotechnology. 27 (2016) 445701.

[38] V.D. Mote, Y. Purushotham, B.N. Dole, Williamson-Hall analysis in estimation of lattice strain in nanometer-sized ZnO particles, J. Theor. Appl. Phys. 6 (2012) 6.

[39] Z.H. Zhou, J. Wang, X. Liu, H.S.O. Chan, Synthesis of Fe3O4 nanoparticles from emulsions, J. Mater. Chem. 11 (2001) 1704–1709.

[40] M.A. López-Quintela, J. Rivas, Chemical reactions in microemulsions: a powerful method to obtain ultrafine particles, J. Colloid Interface Sci. 158 (1993) 446–451.

[41] S. Gangopadhyay, G.C. Hadjipanayis, B. Dale, C.M. Sorensen, K.J. Klabunde, V. Papaefthymiou, A. Kostikas, Magnetic properties of ultrafine iron particles, Phys. Rev. B. 45 (1992) 9778.

[42] E.M. Koushika, C. Balasubramanian, P. Saravanan, G. Shanmugavelayutham, Influence of He and N2 plasma on in situ surface passivated Fe nanopowders by plasma arc discharge, J. Phys. Condens. Matter. 31 (2019) 475302.

[43] G. Xiao, C.L. Chien, Giant magnetic coercivity and percolation effects in granular Fe-(SiO2) solids, Appl. Phys. Lett. 51 (1987) 1280–1282.

[44] E.F. Kneller, F.E. Luborsky, Particle size dependence of coercivity and remanence of single-domain particles, J. Appl. Phys. 34 (1963) 656–658.

[45] I.M.L. Billas, A. Chatelain, W.A. de Heer, Magnetism from the atom to the bulk in iron, cobalt, and nickel clusters, Science (80-.). 265 (1994) 1682–1684.

[46] C. Kittel, Introduction to solid state physics, Wiley New York, 1976.

[47] Y. Ikedo, J. Sugiyama, H. Nozaki, H. Itahara, J.H. Brewer, E.J. Ansaldo, G.D. Morris, D. Andreica, A. Amato, Spatial inhomogeneity of magnetic moments in the cobalt oxide spinel Co 3 O 4, Phys. Rev. B. 75 (2007) 54424.

FIGURES & TABLES

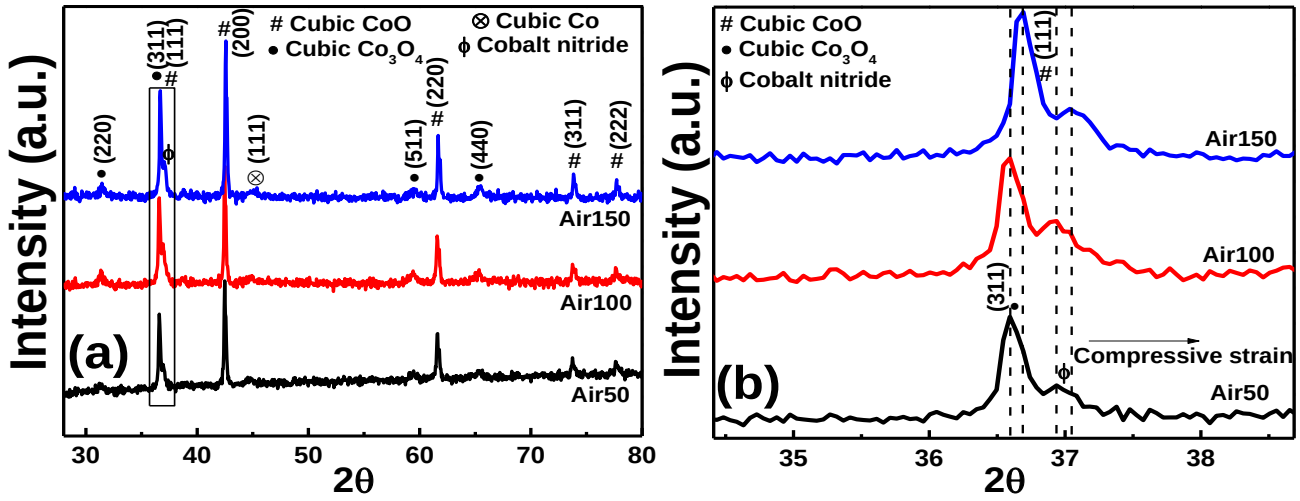

Figure 1: Powder diffraction pattern for (a) Air50, Air100 and Air150 samples and (b) magnified spectra for 2θ between 35°-38°

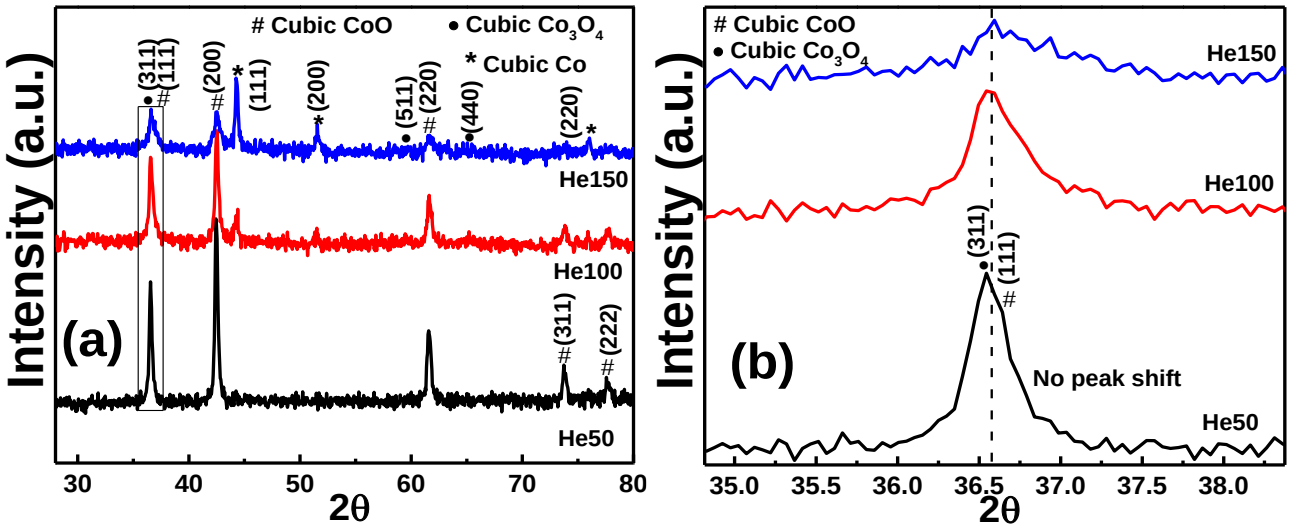

Figure 2: Powder diffraction pattern for (a) He50, He100 and He150 samples and (b) magnified spectra for 2θ between 35°-38°

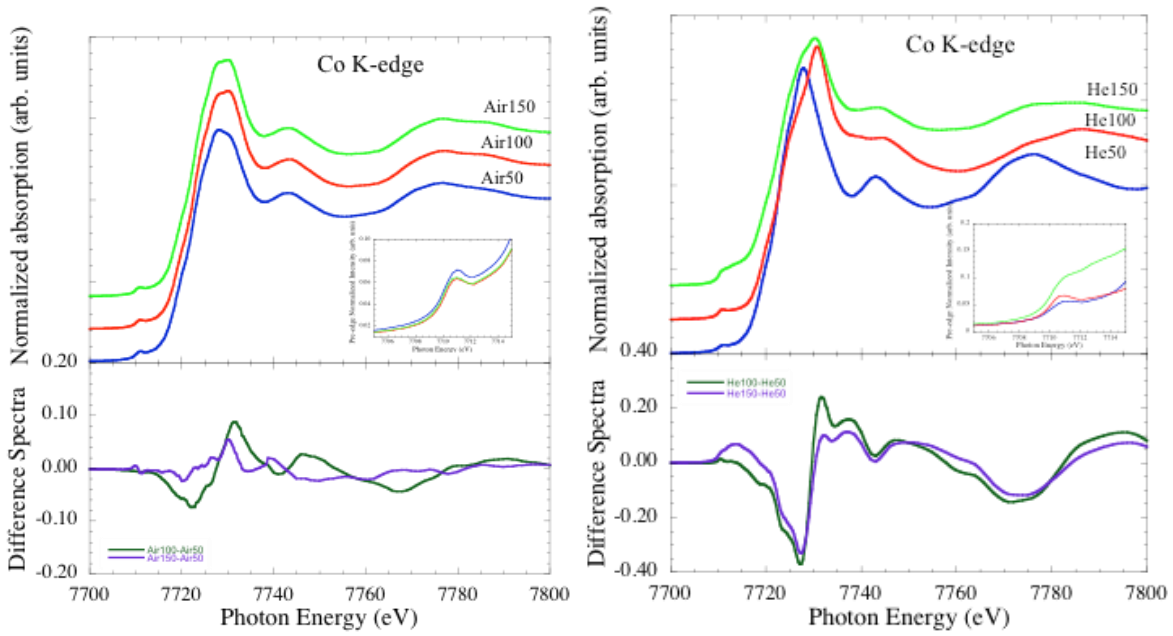

Figure 3: Normalized XANES spectra for (a) Air50, Air100 and Air150 samples and (b) He50, He100 and He150 samples

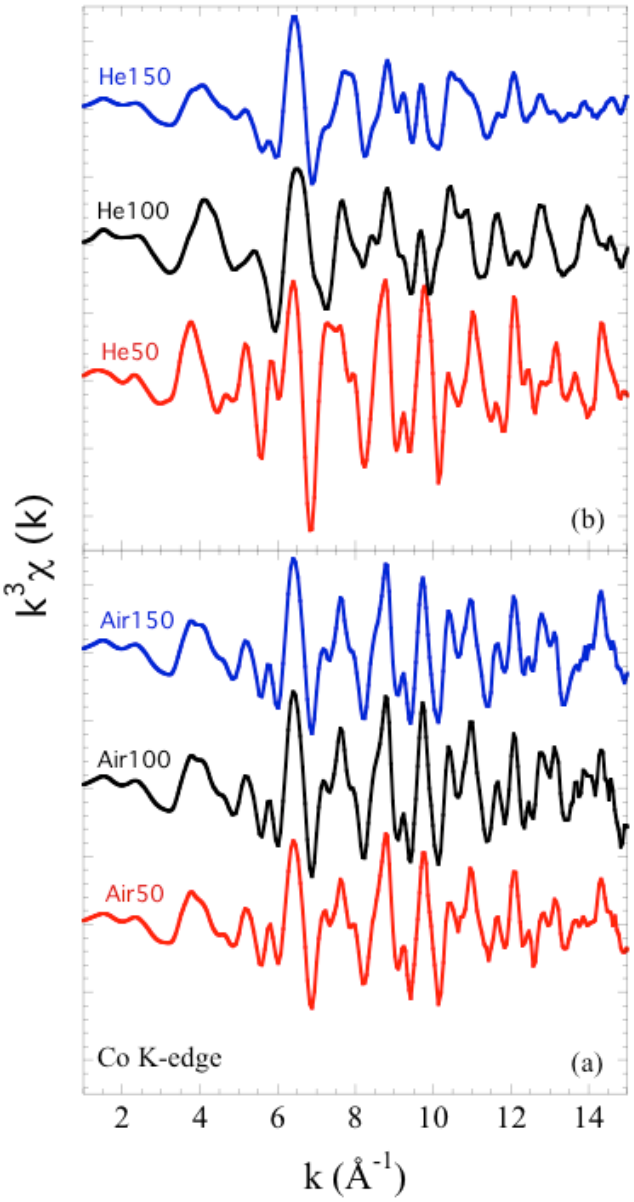

Figure 4: Co K-edge EXAFS oscillations (multiplied by k^3) for the (a) Air and (b) He series of samples.

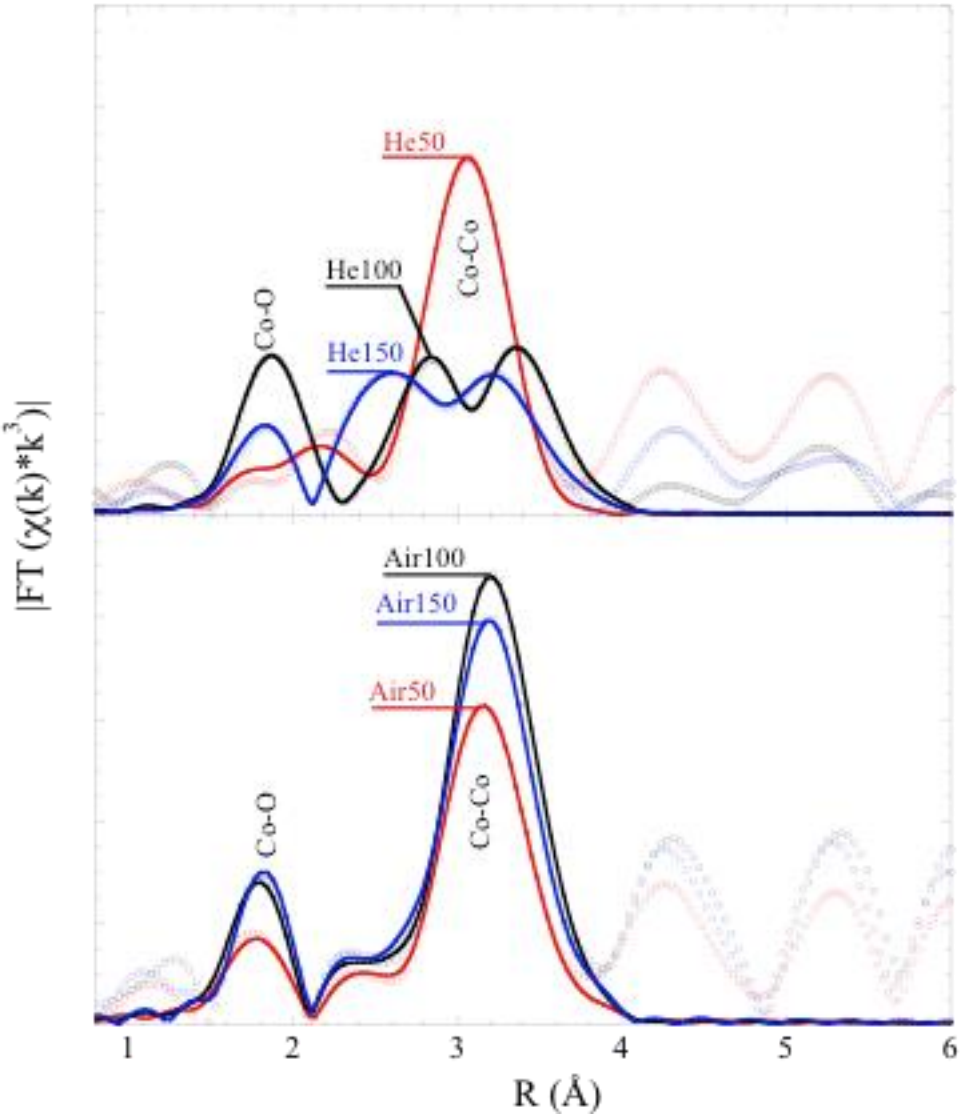

Figures 5: (a) Fourier transform magnitude of □(□) of EXAFS oscillations of Air series of samples (lower); (b) The Fourier transform of He series are shown (upper). The model fits are displayed as solid lines.

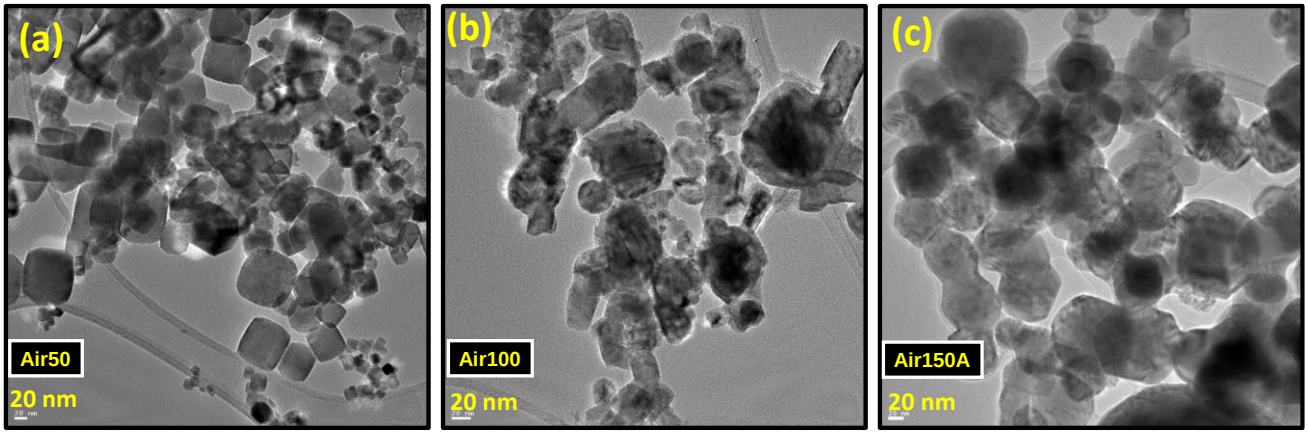

Figure 6: TEM micrographs of (a) Air50 (b) Air100 and (c) Air150 samples

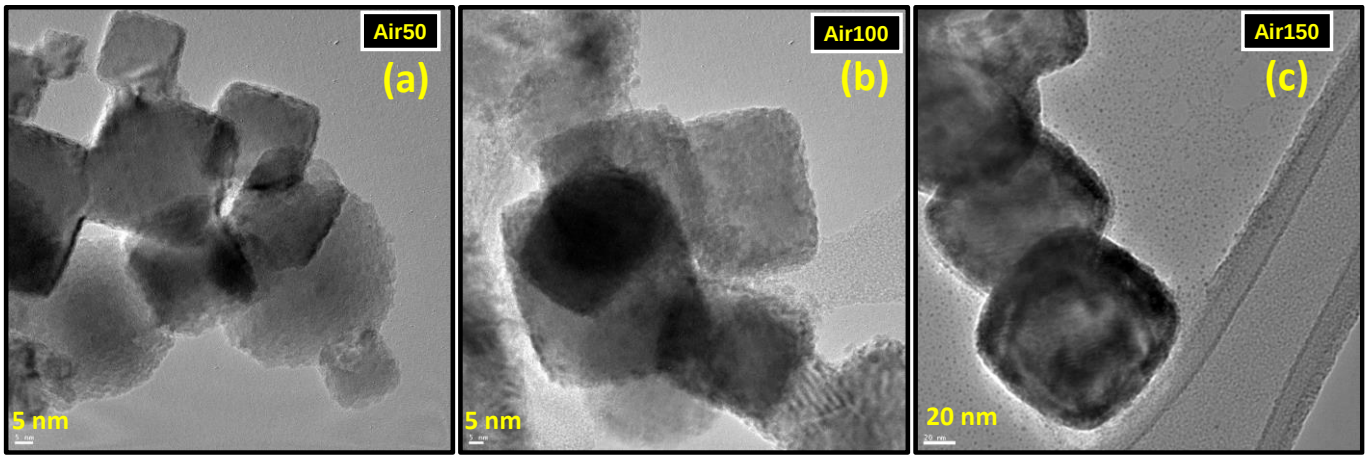

Figure 7: Magnified TEM micrographs of (a) Air50 (b) Air100 and (c) Air150 samples

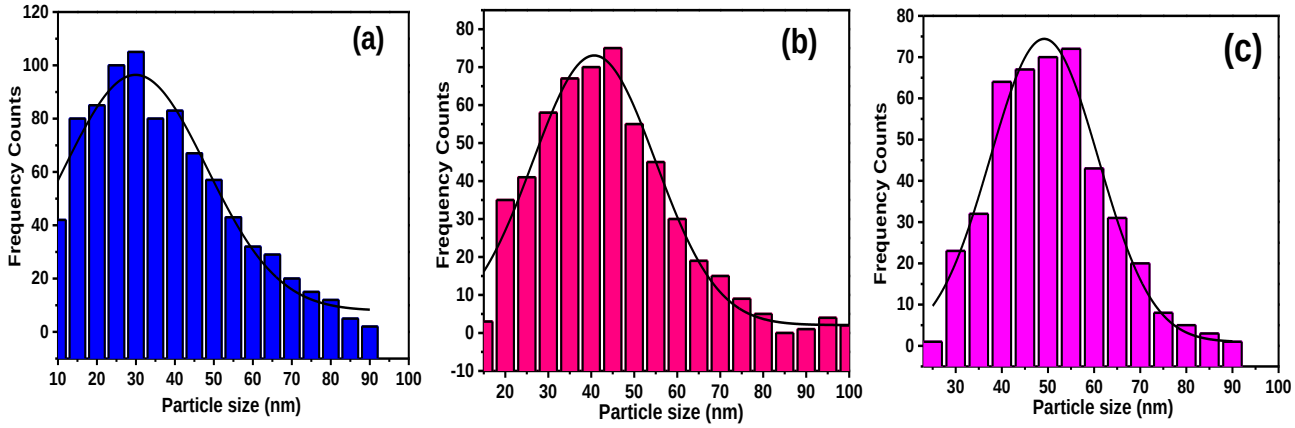

Figure 8: Particle size distribution for (a) Air50 (b) Air100 and (c) Air150 samples

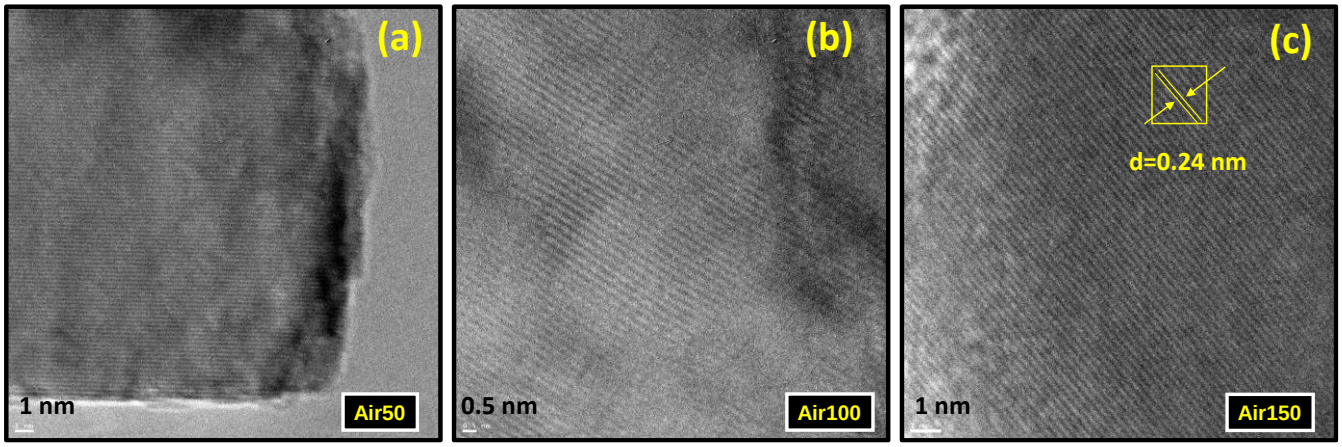

Figure 9: High resolution TEM images showing the atomic planes for (a) Air50 (b) Air100 (c) Air150 samples

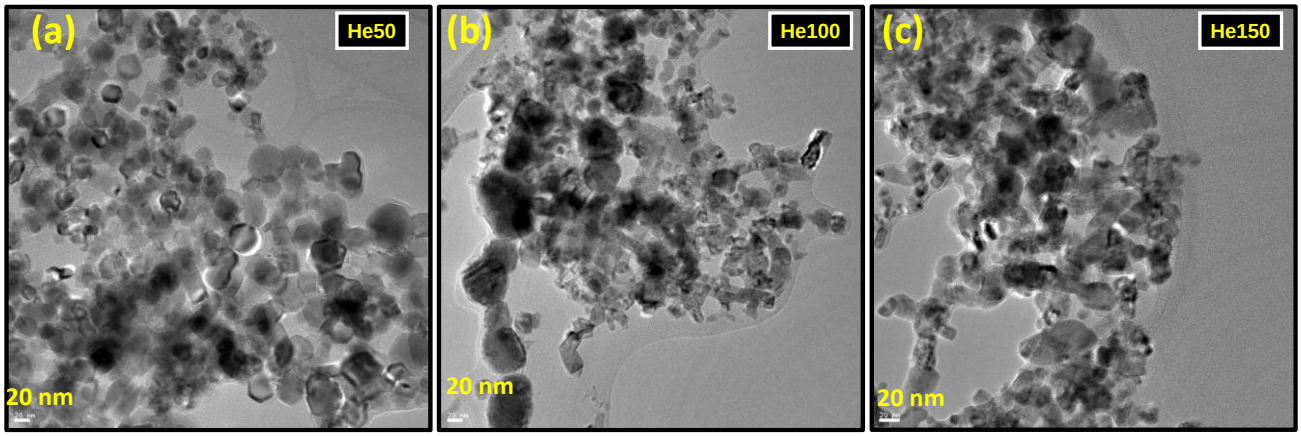

Figure 10: TEM micrographs of (a) He50 (b) He100 and (c) He150 samples

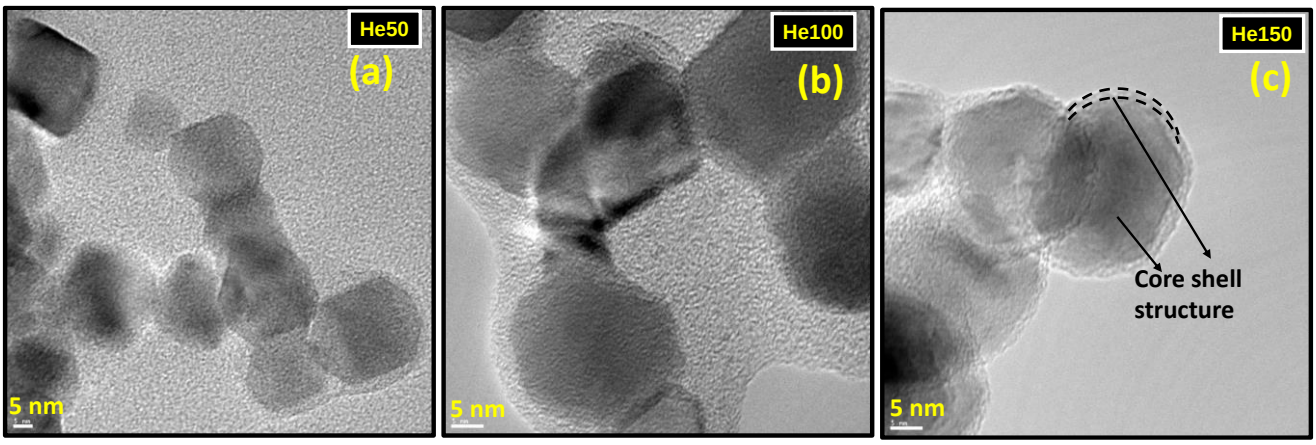

Figure 11: Magnified TEM micrographs of (a) He50 (b) He100 and (c) He150 samples

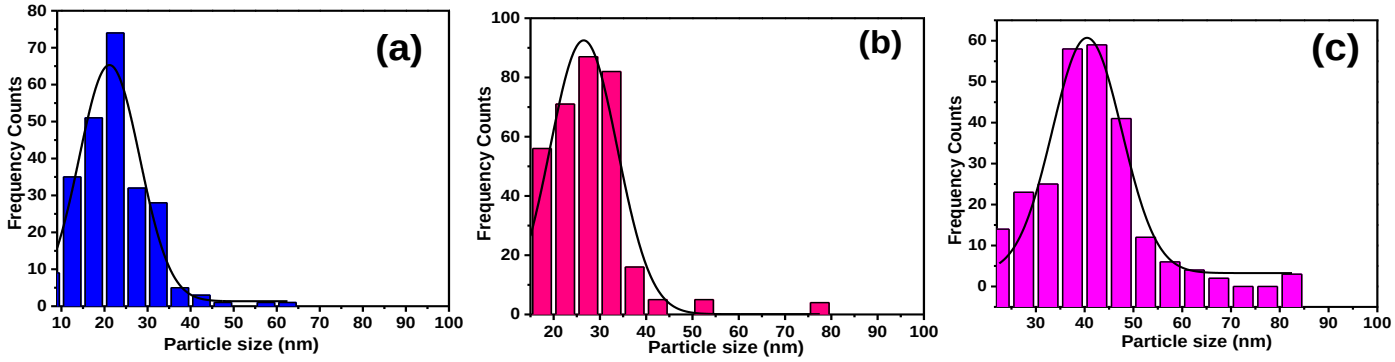

Figure 12: Particle size distribution for (a) He50 (b) He100 and (c) He150 samples

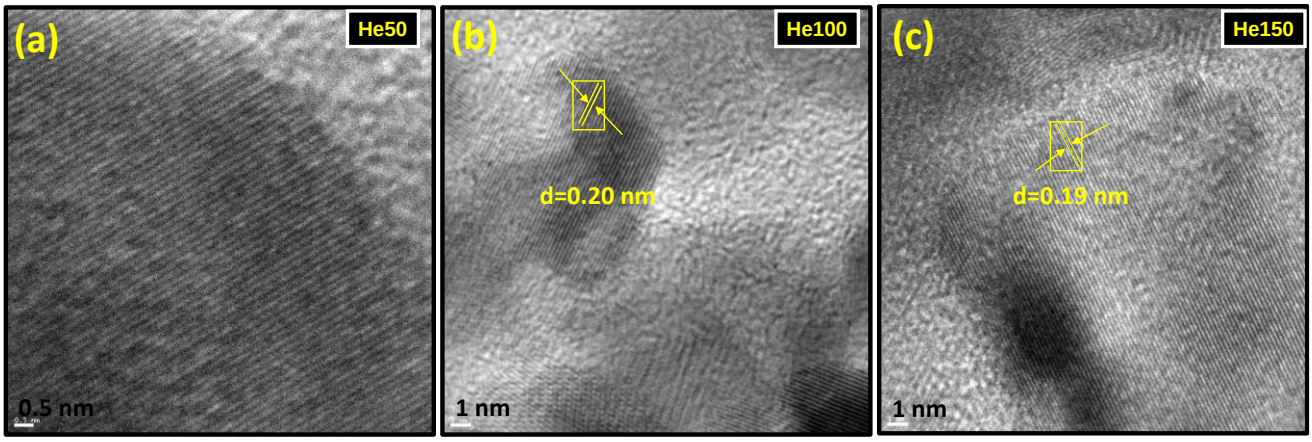

Figure 13: (a, b, c) show the atomic planes for He50, He100 and He150 samples

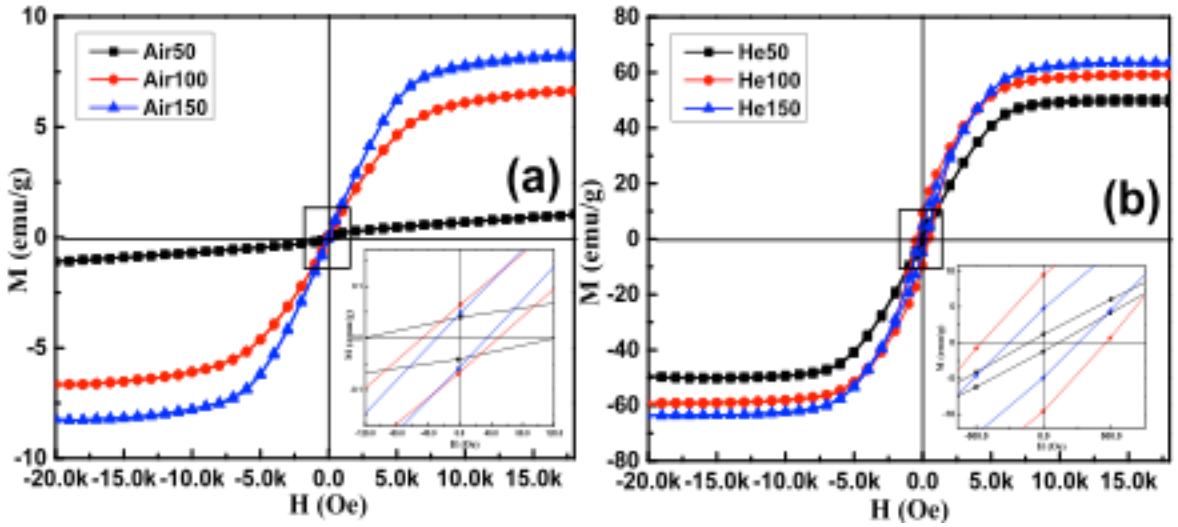

Figure 14: *M* vs *H* loop for (a) Air and (b) He series sample